



Effect of contact interface between TiO_2 and $\text{g-C}_3\text{N}_4$ on the photoreactivity of $\text{g-C}_3\text{N}_4/\text{TiO}_2$ photocatalyst: (001) vs (101) facets of TiO_2

Ze'ai Huang^a, Qiong Sun^b, Kangle Lv^{a,*}, Zehui Zhang^a, Mei Li^a, Bing Li^c

^a Key Laboratory of Catalysis and Materials Science of the State Ethnic Affairs Commission & Ministry of Education, South-Central University for Nationalities, Wuhan 430074, PR China

^b College of Materials Science and Engineering, Qingdao University of Science & Technology, Qingdao 266042, PR China

^c Zhejiang Provincial Key Laboratory of Chemical Utilization of Forestry Biomass, Zhejiang A & F University, Lin'an 311300, PR China

ARTICLE INFO

Article history:

Received 16 June 2014

Received in revised form

18 September 2014

Accepted 21 September 2014

Available online 10 October 2014

Keywords:

Facet-dependent contact

Photoreactivity

High-energy TiO_2

$\text{g-C}_3\text{N}_4$

Z-scheme photocatalyst

ABSTRACT

In this paper, effect of contact interfaces of high-energy TiO_2 , (101) and (001) facets, with $\text{g-C}_3\text{N}_4$ on the photocatalytic activity of $\text{g-C}_3\text{N}_4/\text{TiO}_2$ hybrid was studied using TiO_2 hollow nanobox (TiO_2 -HNB) assembly from high-energy TiO_2 nanosheets (TiO_2 -NS) as model. The prepared photocatalyst was characterized by X-ray diffraction (XRD), transmission electron microscope (TEM), scanning electron microscopy (SEM), nitrogen sorption, Fourier transform infrared spectroscopy (FT-IR), diffuse reflectance spectroscopy (DRS) and X-ray photoelectron spectrometer (XPS). The photoreactivity of the photocatalyst was evaluated by measure the formation rate of photo-induced hydroxyl radicals ($\cdot\text{OH}$) using coumarin as a probe molecule and photocatalytic degradation of Brilliant Red X3B (an anionic dye) under UV irradiation ($\lambda = 365 \pm 10 \text{ nm}$). It was found that $\text{g-C}_3\text{N}_4/\text{TiO}_2$ -HNB forms direct Z-scheme photocatalytic system, which shows superior enhancement on the photocatalytic activity of TiO_2 than $\text{g-C}_3\text{N}_4/\text{TiO}_2$ -NS. It is by contacting $\text{g-C}_3\text{N}_4$ with (101) facets, $\text{g-C}_3\text{N}_4$ can efficient remove the photo-generated electrons accumulated on (101) facets of high-energy TiO_2 , which results in spatially isolated photo-generated electrons and holes, enhancing the photocatalytic activity.

© 2014 Elsevier B.V. All rights reserved.

1. Introduction

Metal oxide semiconductor-mediated photocatalysis has attracted worldwide attention due to its potential in environmental and energy-related applications. However, the rapid recombination rate of photo-generated electron-hole pairs within photocatalytic materials results in its low efficiency, thus limiting its practical applications [1,2]. Recently, control of the crystal facets of semiconductor has attracted enormous interest due to the fascinating shape-dependent photocatalytic activity [3–5]. For example, the study of Yu et al. showed that the {101} and {001} facets of high-energy anatase TiO_2 nanocrystals exhibit different band structures and band edge positions, and the coexposed {101} and {001} facets of anatase can form a “surface heterojunction” within single TiO_2 particle, which is beneficial for the transfer of

photo-generated electrons and holes to {101} and {001} facets, respectively, enhancing the photocatalytic activity [6].

Graphitic carbon nitride ($\text{g-C}_3\text{N}_4$) with layered structure similar to graphene has been reported to be a promising candidate for photocatalysis and electrocatalysis owing to its unique structure and electronic properties [7,8]. The two-dimensional planar structure with π -conjugated system benefits the transport of charge carriers, and the narrow bandgap energy of about 2.7 eV endows the polymeric semiconductor with visible-light absorbing ability up to ca. 460 nm. According to the study of Wang et al., the conduction band (CB) and the valence band (VB) of $\text{g-C}_3\text{N}_4$ were -1.3 V and 1.4 V at pH 7 vs the normal hydrogen electrode (NHE), respectively [9]. Therefore, light-excited electrons in the CB of $\text{g-C}_3\text{N}_4$ possess a large thermodynamic driving force to reduce O_2 ($E_{(\text{O}_2/\cdot\text{O}_2^-)}^\circ = -0.16 \text{ V}$). However, the potential of the photo-generated hole in the VB of $\text{g-C}_3\text{N}_4$ is inadequate to oxidize $-\text{OH}$ to hydroxyl radicals ($E_{(-\text{OH}/\cdot\text{OH})}^\circ = 2.4 \text{ V}$) [9]. Although $\text{g-C}_3\text{N}_4$ has been reported to show photoreactivity for hydrogen production from water splitting [8] and the photo-degradation of organic pollutants [10] under visible light irradiation, the photocatalytic performance of $\text{g-C}_3\text{N}_4$ is

* Corresponding author. Tel.: +86 27 67842752; fax: +86 27 67842752.

E-mail addresses: lvkangle@mail.scuec.edu.cn, lvkangle888@163.com (K. Lv).

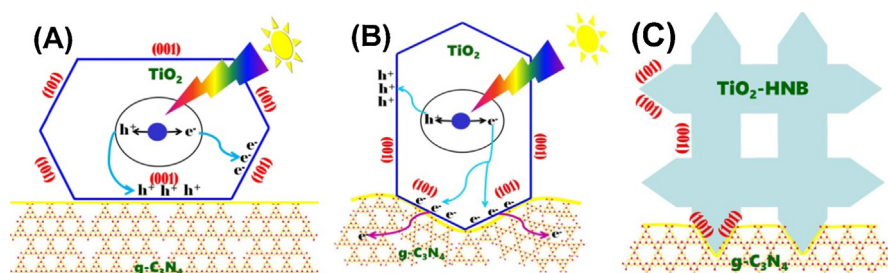


Fig. 1. Comparison on the distributions of photo-generated carriers at contact interface for $g\text{-C}_3\text{N}_4/\text{TiO}_2$ hybrids: contacting $g\text{-C}_3\text{N}_4$ with (001) facets (A) and (101) facets (B). (C) The scheme illustrating that $\text{TiO}_2\text{-HNB}$ mainly contacts $g\text{-C}_3\text{N}_4$ via (101) facets of TiO_2 .

still limited due to the weak oxidative ability of photo-generated hole and quick recombination of the carriers.

To improve the photocatalytic activity of semiconductor photocatalyst, coupling $g\text{-C}_3\text{N}_4$ with TiO_2 [10–12] has attracted much attention. For instance, Yu et al. reported a direct $g\text{-C}_3\text{N}_4/\text{TiO}_2$ Z-scheme photocatalyst prepared by a facile calcination route utilizing affordable P25 TiO_2 and urea as the feedstocks, and they proposed that the photo-induced holes tend to keep in the VB of TiO_2 , while the electrons firstly transfer from the CB of TiO_2 to the VB of $g\text{-C}_3\text{N}_4$, which further excited to its CB [11]. Considering that photo-generated electrons and holes prefer to migrate to (101) and (001) facets of high-energy TiO_2 nanocrystals, respectively, contacting $g\text{-C}_3\text{N}_4$ with (101) instead of (001) facets of TiO_2 should facilitates the removal of photo-generated electrons of TiO_2 , therefore enhancing the photocatalytic activity (compare Fig. 1A and B). Unfortunately, such facet-dependent contact $g\text{-C}_3\text{N}_4/\text{TiO}_2$ hybrid photocatalyst has not been reported. One possible reason is that it is hard to control the contact facets of high-energy TiO_2 nanocrystals such as (001) and (101) with two-dimensional planar structured $g\text{-C}_3\text{N}_4$.

Our group has reported the fabrication of a TiO_2 hollow nanobox ($\text{TiO}_2\text{-HNB}$) assembly from anatase TiO_2 nanosheets ($\text{TiO}_2\text{-NS}$) with both exposed (101) and (001) facets [13]. The unique structures of $\text{TiO}_2\text{-HNB}$ makes it possible to contact $g\text{-C}_3\text{N}_4$ with (101) facets of high-energy TiO_2 (Fig. 1C). Herein, we modified $\text{TiO}_2\text{-HNB}$ with $g\text{-C}_3\text{N}_4$ by a facile one-pot solvothermal strategy using TiOF_2 cubes and $g\text{-C}_3\text{N}_4$ as starting materials, and the facet-dependent contact on the photoreactivity of $g\text{-C}_3\text{N}_4/\text{TiO}_2$ hybrid was systematically studied.

2. Experimental

2.1. Materials

Dicyandiamide was obtained from Aladdin Chemical Reagent Corp., PR China. Tetrabutyl titanate (TBT), hydrofluoric acid (40 wt.%), acetate acid (>99.8%) and *tert*-butyl alcohol (TBA) were purchased from Beijing Chem. Works, PR China. All chemicals were used as received without further purification, and ultrapure water (>18 M Ω cm) obtained from Millipore system was used throughout all the experiments.

2.2. Preparation of $g\text{-C}_3\text{N}_4$

The $g\text{-C}_3\text{N}_4$ powder was synthesized according to the literature [7]. Specifically, 20.0 g of dicyandiamide was put into an alumina crucible with a cover, which was then heated in a muffle furnace at a rate of 10 $^\circ\text{C min}^{-1}$ and kept for 3 h at 550 $^\circ\text{C}$. After cooled to room temperature, the resulted yellow product was collected and ground into powder for further use.

2.3. Fabrication of $g\text{-C}_3\text{N}_4/\text{TiO}_2$ hybrid

Precursor TiOF_2 was prepared by a microwave-assisted synthetic strategy according to our previous report [13]. The $g\text{-C}_3\text{N}_4/\text{TiO}_2\text{-HNB}$ hybridized composites were prepared through a solvothermal strategy using TBA as solvent. Typically, 2.0 g of TiOF_2 and certain amount of $g\text{-C}_3\text{N}_4$ (0–1.0 g) were added into a beaker containing 40 mL of TBA under magnetic stirring, and the resulted suspensions were transferred into a Teflon-lined autoclave after ultrasonicated for 10 min. Then the autoclave was heated at 180 $^\circ\text{C}$ for 5 h in an oven. After cooled down to room temperature, the products were filtrated through a membrane filter (pore size 0.45 μm). To eliminate the surface adsorbed fluoride ions, the precipitate was firstly washed by NaOH solution (0.1 mol L^{-1}), and then by distilled water till the pH value of the filtrate is about 7 [14]. The resulted sample after drying in a vacuum oven at 80 $^\circ\text{C}$ for 6 h was labeled as “TBx”, where “TB” refers box-like morphology of TiO_2 and “x” represents the amount of $g\text{-C}_3\text{N}_4$ used (Table 1). For example, TB0.2 refers the sample prepared from 2.0 g of TiOF_2 and 0.2 g $g\text{-C}_3\text{N}_4$. The pure $\text{TiO}_2\text{-HNB}$ sample, prepared in the absence of $g\text{-C}_3\text{N}_4$ powder, was simply denoted as TB0.

2.4. Characterization

The X-ray diffraction (XRD) patterns of the samples were obtained on a D8 advance X-ray diffractometer (Germany Bruker) using Cu K α radiation at a scan rate (2θ) of 0.05 $^\circ\text{s}^{-1}$. The voltage and applied current were 40 kV and 80 mA, respectively. The morphology of the photocatalyst was observed on a transmission electron microscopy (TEM) (Tecnai G20, USA) using an acceleration voltage of 200 kV and a field emission scanning electron microscope (SEM) (Hitach, Japan) with an acceleration voltage of 10 kV, respectively. Nitrogen adsorption–desorption isotherms were obtained on an ASAP 2020 (Micromeritics Instruments, USA) nitrogen adsorption apparatus. All the samples were degassed at 120 $^\circ\text{C}$ prior to Brunauer–Emmett–Teller (BET) measurements. The BET specific surface area (S_{BET}) was determined by a multipoint BET method using the adsorption data in the relative pressure P/P_0 range of 0.05–0.30. The desorption isotherm was used to determine the pore size distribution by using the Barret–Joyner–Halenda (BJH) method. The nitrogen adsorption volume at $P/P_0 = 0.994$ was used to determine the pore volume (PV) and average pore size (APS). Fourier transform infrared spectroscopy (FT-IR) was recorded on a NEXUIS-470 infrared spectrometer (Nicolet Co., USA). Diffuse reflectance spectroscopy (DRS) of the photocatalyst was obtained from the dry-processed disk samples using a UV–vis spectrophotometer (Lambda, Bio 35, PE Co., USA). X-ray photoelectron spectroscopy (XPS) measurement was done using Multilab 2000 XPS system with a monochromatic Mg K α source and a charge neutralizer, all the binding energies were

Table 1
Physical properties of the photocatalyst.

Sample	Starting materials		Characterization results		
	TiOF ₂ (g)	g-C ₃ N ₄ (g)	S _{BET} (m ² g ⁻¹)	PV (cm ³ g ⁻¹)	APS (nm)
TB0	2.0	0	47.7	0.11	9.3
TB0.05	2.0	0.05	53.9	0.14	10.0
TB0.2	2.0	0.2	61.6	0.17	11.3
TB0.5	2.0	0.5	68.1	0.22	12.9
TB1	2.0	1.0	73.7	0.23	12.6
g-C ₃ N ₄	–	–	32.6	0.24	29.8

referenced to the C1s peak at 284.4 eV of the surface adventitious carbon.

2.5. Evaluation of the photocatalytic activity

The photocatalytic activity of the photocatalyst was evaluated both by measure the formation of hydroxyl radicals ($\cdot\text{OH}$) and photocatalytic degradation of Brilliant Red X-3B (X3B), an anionic dye, under UV irradiation. The formation of $\cdot\text{OH}$ radicals in solution was performed by a photoluminescence (PL) technique using coumarin as a probe molecule, which readily reacted with $\cdot\text{OH}$ radicals to produce highly fluorescent product, 7-hydroxycoumarin [15,16]. The suspensions of TiO₂ (1.0 g L⁻¹) containing coumarin (0.5 mmol L⁻¹) were mixed under magnetic stirring, and then shaken overnight. At given intervals of irradiation under a 3 W LED lamp (emitted mainly at 365 ± 10 nm), small aliquots were withdrawn by a syringe, and filtered through a membrane (pore size 0.45 μm). The filtrate was analyzed on a Hitachi F-7000 fluorescence spectrophotometer by the excitation with the wavelength of 332 nm.

The procedure for photocatalytic degradation of X3B, initial concentration of 1.0 × 10⁻⁴ mol L⁻¹, is similar to $\cdot\text{OH}$ radicals measurement, except that the concentration of X3B remaining in the filtrate was analyzed by an Agilent 8451 spectrometer at 510 nm.

2.6. Photoelectrochemical measurements

Photocurrent was measured on an electrochemical analyzer (CHI660D Instruments) in a standard three-electrode system using the prepared samples as the working electrodes with an active area of ca. 0.5 cm², a Pt wire as the counter electrode, and saturated calomel electrode (SCE) as a reference electrode [17]. A continuous solar simulator (100 mW cm⁻², Newport 96000) through a spherical filter (AM 1.5G, Newport 81094) served as a light source. Na₂SO₄ (0.1 mol L⁻¹) aqueous solution was used as the electrolyte. Working electrodes were prepared as follows: 1.8 wt.% of photocatalyst were ground with 5 wt.% of polyvinyl alcohol (PVA) and 0.5 mL of water to make a slurry. The slurry was then coated onto a 2.0 cm × 1.2 cm F-doped SnO₂-coated glass (FTO glass) electrode by the doctor blade technique. Next, these electrodes were dried in an oven and calcined at 450 °C for 30 min. SEM image showed that the thickness of the film on FTO glass was about 10 μm (not shown here).

2.7. Powder photoluminescence spectra

Photoluminescence (PL) spectra were measured at room temperature on a Fluorescence Spectrophotometer (F-7000, Hitachi, Japan). The excitation wavelength was 300 nm. Both of the width for excitation and emission slits were 5.0 nm. The scanning speed was 1200 nm min⁻¹ and the photomultiplier tube (PMT) voltage was 700 V.

3. Results and discussion

3.1. Phase structure and morphology

Fig. 2 shows the XRD patterns of the prepared photocatalysts. It can be seen from Fig. 2a that a typical peak at $2\theta = 23.4^\circ$, corresponding to the (1 0 0) plane diffraction of TiOF₂ (JCPDS No. 08-0060), was observed for TiO₂ precursor, and no peaks of any anatase phase TiO₂ exists, which indicates that the precursor is pure phase TiOF₂ [18,19]. As for pure g-C₃N₄, two peaks at $2\theta = 27.4^\circ$ and 13.1° , corresponding to the (0 0 2) and (1 0 0) diffraction planes of g-C₃N₄, were observed (Fig. 2g) [11]. After solvothermal treated at 180 °C for 5 h, precursor TiOF₂ successfully transforms to pure anatase TiO₂ (Fig. 2b for TB0). As for g-C₃N₄/TiO₂-HNB hybridized composites, similar characteristic diffraction peaks of anatase TiO₂ as TB0 are observed, implying that the presence of g-C₃N₄ has no significant influence on the phase transformation of TiOF₂ to anatase TiO₂ (Fig. 2c–f). However, small characteristic diffraction peaks of g-C₃N₄ were also observed for TB0.5 sample (Fig. 2e), and the peaks of g-C₃N₄ in TB1 sample becomes more obviously (Fig. 2f), confirming the coexistence of anatase TiO₂ and g-C₃N₄ in the hybrid.

The morphology and microstructure of as-prepared samples were further investigated by TEM (Fig. 3) and SEM images (Fig. 4). Fig. 3a shows the crumpled layered structure of pure g-C₃N₄, which possibly contains several stacking layers, indicating the planar graphitic-like structure. Compared with the morphology of pure g-C₃N₄, box-like materials with hollow interiors (see red arrow), were found to disperse on the crumpled g-C₃N₄ film (see white arrow). The box-like materials should be TiO₂-HNB, which were transformed from TiOF₂ cubes (Fig. 2b–f) [13,20]. The sidelength of TiO₂-HNB is about 200–300 nm, consistent with that of the precursor (cubic TiOF₂). Our previous studies have clearly

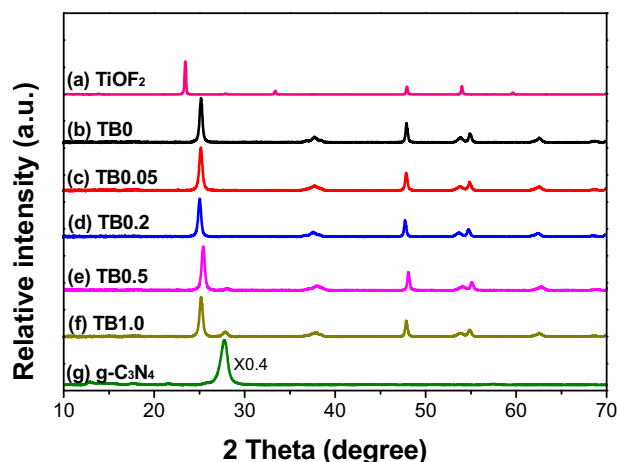


Fig. 2. XRD patterns of the prepared photocatalysts.

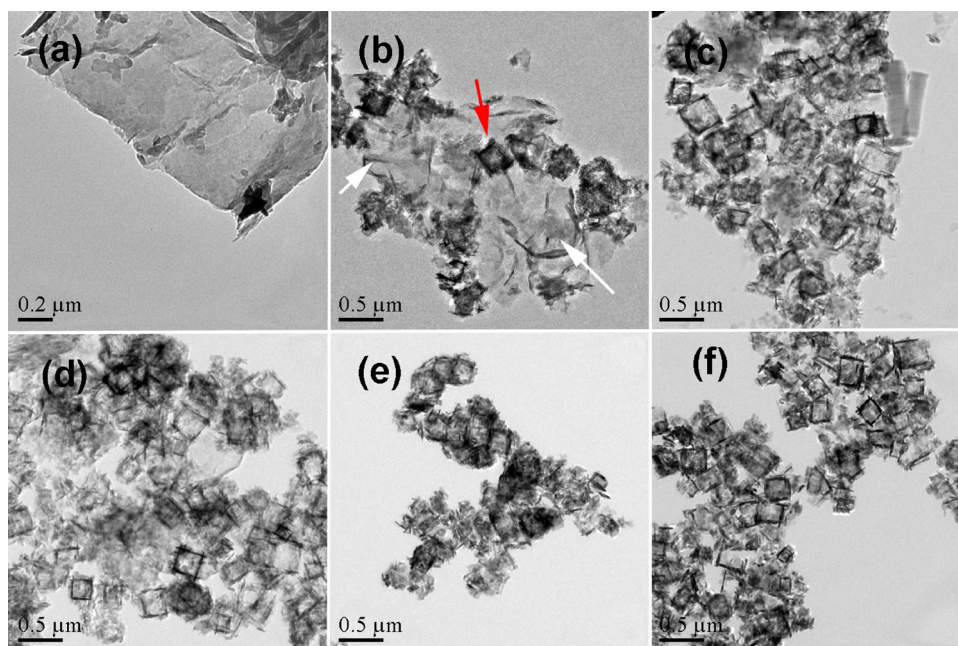


Fig. 3. TEM images of g-C₃N₄ (a), TB1 (b), TB0.5 (c), TB0.2 (d), TB0.05 (e), and TB0 (f), respectively. Red and white arrows in image (b) showing the presence of hollow structured TiO₂ nanobox and film-like g-C₃N₄, respectively. (For interpretation of the references to color in this figure legend, the reader is referred to the web version of this article.)

shown that the phase transformation of TiOF₂ cube to TiO₂-HNB is *via in situ* dissolution–recrystallization process, and the TiO₂-HNB are assembly from high-energy TiO₂-NS with exposed both (101) and (001) facets [13]. TEM image shows that TiO₂-NS prefers to lay on the surface of g-C₃N₄, contacting g-C₃N₄ with (001) facets (Fig. S1). However, the unique structures of TiO₂-HNB makes TiO₂-NS contact layered g-C₃N₄ with (101) facets (Fig. 1C and 4). From Fig. 3b–f, it can be seen that the number density of TiO₂-HNB increases with decreasing the amount of g-C₃N₄.

From Fig. 4, it can be seen that some of the TiO₂-HNBs were deeply wrapped by g-C₃N₄ films, reflecting the strong reaction between (101) facets of TiO₂-HNB and g-C₃N₄. Compared with (001) facets, (101) facets TiO₂-NS in TiO₂-HNB should have more chance to contact film-like g-C₃N₄. Since photo-generated electrons prefer to migrate to (101) facets of TiO₂-NS, the strong reaction between (101) facets of TiO₂ with g-C₃N₄ should facilitate the efficient removal of photo-generated electrons accumulate on (101) facets, leaving holes left on (001) facets. This efficient spacial separation of photo-generated electron-hole pairs in g-C₃N₄/TiO₂-HNB hybrid should benefit the photocatalytic activity (Fig. 1).

3.2. Nitrogen sorption

The BET surface areas and porous structures of the photocatalysts were investigated by nitrogen adsorption–desorption. Fig. 5 shows the nitrogen adsorption–desorption isotherms and the corresponding pore-size distribution curves (inset) of pure TiO₂-HNB (TB0) and g-C₃N₄/TiO₂-HNB hybrids (TB0.2 and TB1). It can be seen that all the photocatalysts have isotherms of type IV according to the Brunauer–Deming–Deming–Teller (BDDT) classification, indicating the presence of mesopores (2–50 nm). The shapes of the hysteresis loops are of type H3 at a high relative pressure range of 0.8–1.0, indicating the presence of slit-like pores, which is consistent with the morphology of TiO₂-HNB assembly from TiO₂-NS [13].

The pore distributions of the photocatalysts are very broad (inset in Fig. 5), and the BET specific surface areas of the as-prepared sample increases from 47.7 m² g^{−1} (TB0) to 73.7 m² g^{−1} (TB1) with increasing amounts of g-C₃N₄. The BET surface area of g-C₃N₄ was measured to be 32.6 m² g^{−1} (Table 1 and Fig. S2), which is smaller than that of TiO₂-HNB (47.7 m² g^{−1}). Why the BET specific surface areas of g-C₃N₄/TiO₂-HNB hybrid increases with increasing the

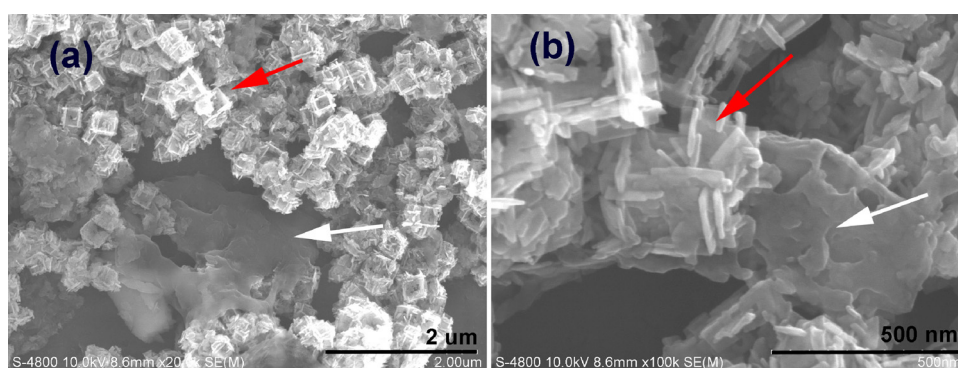


Fig. 4. Low (a) and high (b) resolution SEM images of TB0.2 sample. Red and white arrows indicating the presence of TiO₂ hollow nanobox and film-like g-C₃N₄, respectively. (For interpretation of the references to color in this figure legend, the reader is referred to the web version of this article.)

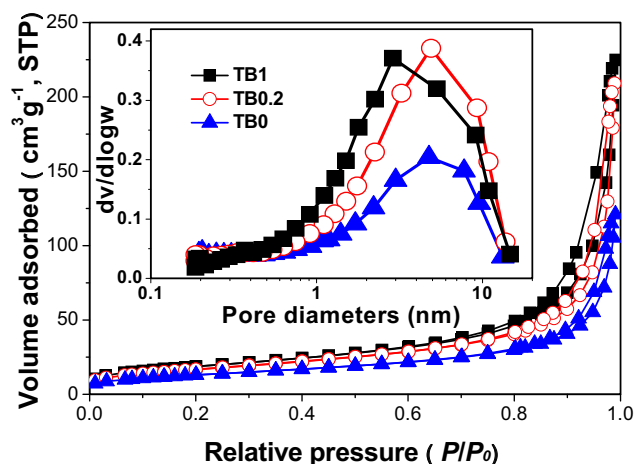


Fig. 5. Nitrogen adsorption-desorption isotherms and the corresponding pore size distributions (inset) of the photocatalysts.

amount of g-C₃N₄? Our preliminary results showed that g-C₃N₄ can be exfoliated in HF solution (Fig. S3), resulting in enlarged BET specific areas. However, this needs to be studied further. The increased specific surface areas due to g-C₃N₄ exfoliation are beneficial for enhancing the photocatalytic activity of the hybrids.

3.3. FT-IR analysis

The FT-IR spectra of g-C₃N₄, TiO₂-HNB and g-C₃N₄/TiO₂-HNB hybrid are shown in Fig. 6. For pure TiO₂-HNB, three main absorption regions can be clearly observed (Fig. 6a). The broadband peak at 3300–3500 cm⁻¹ is attributed to the O–H stretching of physisorbed water on the surface of TiO₂, and the relatively sharp band at 1637 cm⁻¹ corresponds to the O–H bending modes of water molecules. The strong absorption observed below 850 cm⁻¹ could be attributed to the absorption of Ti–O–Ti [21]. Three main absorption regions were also observed for pristine g-C₃N₄ (Fig. 6d), where the broad peak at 3000–3300 cm⁻¹ is ascribed to the stretching vibration of N–H, and the strong band of 1200–1600 cm⁻¹, with the characteristic peaks at 1241, 1319, 1403, 1465, and 1573 cm⁻¹, is attributed to the typical stretching vibration of C–N heterocycles, and the peak at 810 cm⁻¹ can correspond to the breathing mode of triazine units [22].

As expected, all the main absorption peaks of g-C₃N₄ and TiO₂ appear in the spectra of the g-C₃N₄/TiO₂-HNB hybrid, but in low

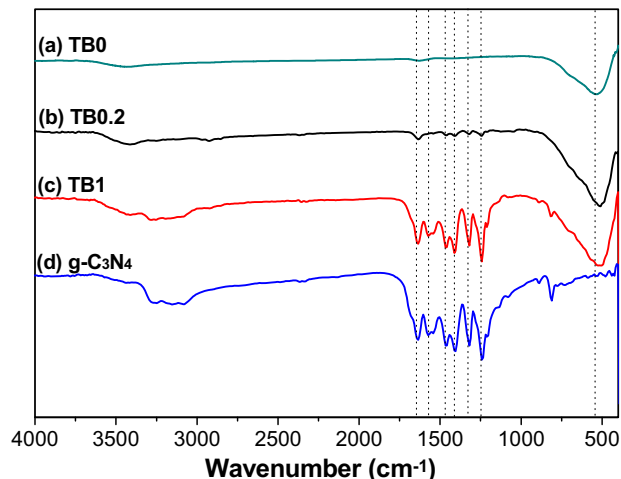


Fig. 6. FT-IR spectra of the prepared photocatalysts.

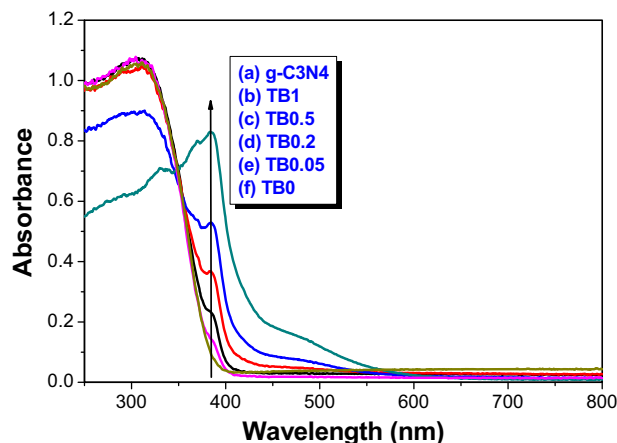


Fig. 7. UV-Vis diffuse reflectance spectra of the photocatalysts.

intensity. Compared with the absorption band of Ti–O–Ti stretching vibration for pure TiO₂-HNB (peak at 527 cm⁻¹), the slight shift of this Ti–O–Ti vibration mode in TB0.2 hybrid (peak at 516 cm⁻¹) was observed, implying the interfacial interaction between g-C₃N₄ layers and TiO₂-HNB. This strong interfacial interaction between g-C₃N₄ layers and TiO₂-HNB would facilitate the electron transfer, and therefore improve the photocatalytic efficiency [11].

3.4. UV-Vis diffuse reflectance spectrum

The absorbance properties of the photocatalysts were measured using UV-Vis diffuse reflectance spectroscopy (Fig. 7). For pure TiO₂-HNB, the absorption occurs at wavelengths shorter than 400 nm, consistent with the intrinsic band gap of anatase TiO₂ (about 3.2 eV), while the absorption intensity of pure g-C₃N₄ rises rapidly at about 450 nm, in good accordance with the band gap of g-C₃N₄ (2.7 eV). Compared with pure TiO₂-HNB (TB0), the g-C₃N₄/TiO₂-HNB hybrids show additional absorption in the region of ca. 400–430 nm, attributed to the existence of g-C₃N₄. In the other regions, TB0 and TB1 samples exhibit similar absorption features, indicating that carbon or nitrogen elements are not incorporated into the lattice of TiO₂-HNB. Therefore, the g-C₃N₄ in the hybrid only deposits on the surface of the TiO₂-HNB instead of being incorporated into the lattice.

3.5. XPS analysis

XPS technique was further employed to characterize the elemental composition and bonding configurations in g-C₃N₄/TiO₂-HNB hybridized composites. According to XPS survey spectrum shown in Fig. 8A, TiO₂-HNB (TB0) sample only contains Ti, O and C elements, with sharp photoelectron peaks appearing at binding energies of 458.2 (Ti 2p), 529.5 (O 1s) and 284.6 eV (C 1s), respectively. The carbon peak is attributed to the residual carbon from the sample and adventitious hydrocarbon from XPS instrument itself. However, the peak of N 1s of g-C₃N₄/TiO₂-HNB hybrid was observed at the corresponding high-resolution spectrum (Fig. 8B). The asymmetrical and broad features of the observed N 1s XPS spectrum of g-C₃N₄/TiO₂-HNB hybrid suggest the coexistence of distinguishable models. The signal can be deconvoluted into two obvious peaks at 398.7 and 399.2 eV, which can be ascribed to the sp²-hybridized pyridine N nitrogen (C=N–C) and tertiary pyrrolic nitrogen (N–C₃), respectively [7]. The N 1s peak of g-C₃N₄ can be deconvoluted three fitted peaks at 398.3, 399.2, and 400.7 eV, which are assigned to the pyridine N, pyrrolic N, and graphitic N, respectively. The binding energy of pyridine N in g-C₃N₄/TiO₂-HNB sample (398.7 eV) increased 0.4 eV when compared with that of

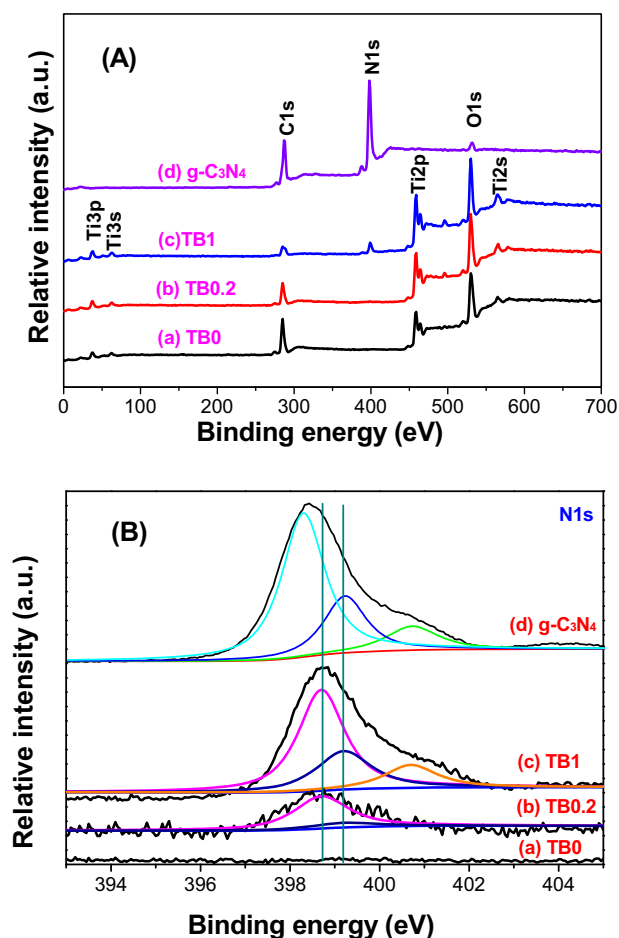


Fig. 8. XPS survey spectra of the photocatalysts (A) and the corresponding core levels of N 1s (B) region.

pristine g-C₃N₄ (398.3 eV), also reflecting the interfacial interaction between g-C₃N₄ and TiO₂-HNB (Fig. 8B).

3.6. Photocatalytic performance

It has been reported that various reactive oxidation species, such as O₂^{•−}, ¹O₂ (a¹Δ_g), •OH, and H₂O₂, are generated on the TiO₂ surface in the gas and liquid phases [23]. Among them, •OH radical is an extremely important species and it has been proposed to be the responsible for many oxidation pathways of chemical compounds initiated through heterogeneous photocatalytic processes. The yield of •OH radicals depends on the competition between oxidation of surface water by the holes and electron-hole recombination. Therefore, the measurement of •OH radicals is helpful to understand the mechanism of photocatalysis. In this work, we used coumarin as a probe to evaluate the photocatalytic activity of the photocatalysts, which readily reacted with •OH radical to produce highly fluorescent product, 2-hydroxyterephthalic acid [24].

Fig. 9A shows the PL intensity at 450 nm against the irradiation time in the presence of the photocatalyst. It can be seen that the generation of fluorescent 7-hydroxycoumarin is linearly proportional to illumination time, obeying a pseudo-zero-order reaction rate equation in kinetics. The rate constant, which represents the photocatalytic activity of the photocatalysts, increases first and then decreases with increasing the amount of g-C₃N₄. Pure g-C₃N₄ shows very poor UV photocatalytic activity (rate constant of only 2.17). This is due to the failure oxidization of −OH to •OH radicals ($E^{\circ}(-\text{OH}/\bullet\text{OH}) = 2.4 \text{ V}$) by photo-generated hole of g-C₃N₄ [9].

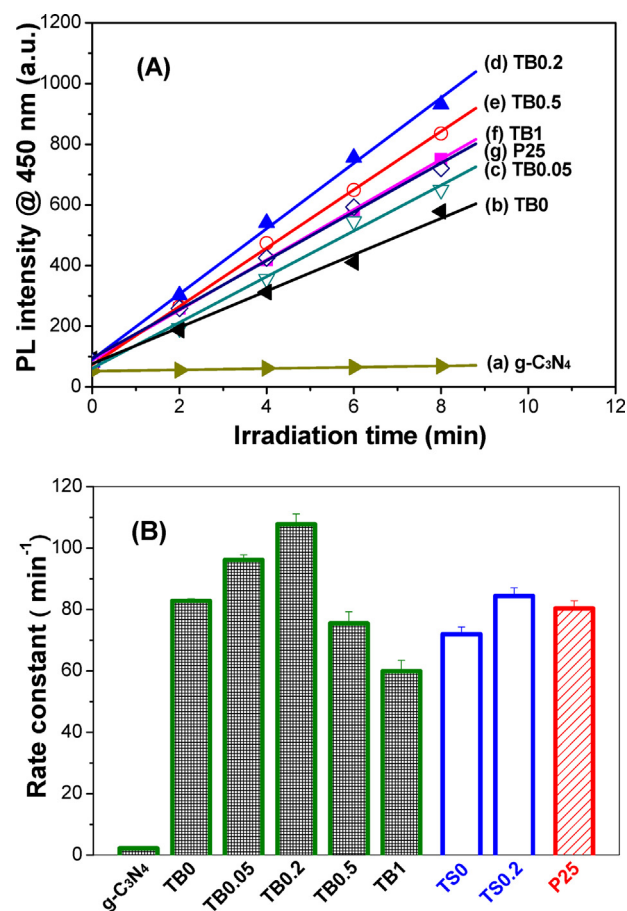


Fig. 9. Time dependence of the induced photoluminescence intensity @ 450 nm of the photocatalysts (A) and comparison of the corresponding rate constants (B).

Therefore, it is not strange to see that little •OH radicals were detected in illuminated g-C₃N₄ suspensions.

Although TB0 shows excellent photocatalytic activity with a rate constant of 82.82, the photocatalytic activity of TiO₂-HNB hybrid was found to be improved after coupling with g-C₃N₄. TB0.2 (rate constant of 107.76) shows the highest photocatalytic activity among all the g-C₃N₄/TiO₂-HNB hybridized composites, which is 30% and 34% times higher than that of TB0 and commercial P25 TiO₂ (rate constant of 80.33), respectively. Considering that TiO₂-HNB was assembled from discrete high-energy TiO₂-NS, effect of g-C₃N₄ on the photocatalytic activity of TiO₂-NS was therefore studied. It was found that, after modified with same weight ratio of g-C₃N₄ as that of TB0.2, the photocatalytic activity of TiO₂ nanosheets (TS0.2) only enhanced by a factor of 17% (71.92 for TS0 and 84.40 for TS0.2).

Why TB0.2 shows higher photocatalytic activity than TS0.2? This is because TiO₂-HNB contact g-C₃N₄ via (1 0 1) facets, while discrete TiO₂-NS via (0 0 1) facets (Fig. 1 and Fig. S1). As discussed above, photo-generated electrons prefers to migrate to (1 0 1) facets of high-energy TiO₂. By contacting g-C₃N₄ with (1 0 1) facets, TiO₂-HNB shows higher efficiency in removal of the photo-generated electrons accumulated on the surface of TiO₂. Therefore, it is not hard to understand the high photocatalytic activity of TB0.2 hybrid. The experimental results suggest the importance of contact interface in design of hybridized catalyst (facet-dependent).

Fig. 10 shows the degradation profiles of X3B dye using TB0 and TB0.2 as photocatalyst, respectively. The kinetic data for the degradation of X3B can be well fitted by the apparent first-order rate equation, and the degradation rate constant of X3B increased

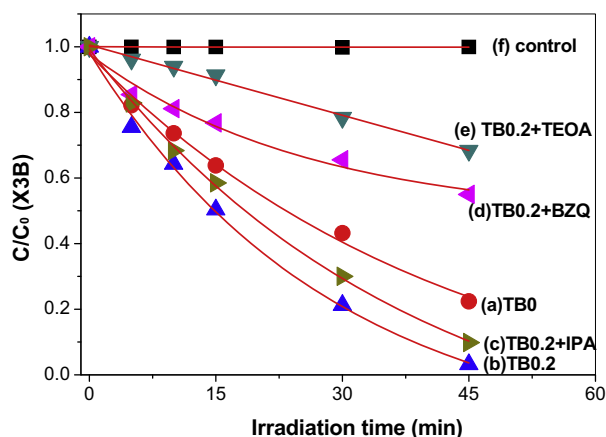


Fig. 10. Photocatalytic degradation profiles of X3B dye.

from 0.031 min^{-1} (TB0) to 0.051 min^{-1} (TB0.2) after coupling TiO_2 -HNB with $\text{g-C}_3\text{N}_4$. This is consistent with the trend of $\cdot\text{OH}$ radicals formation rate (Fig. 9).

3.7. Photocurrent and powder photoluminescence

To account for the positive effect of $\text{g-C}_3\text{N}_4$ on the enhanced photocatalytic activity of $\text{g-C}_3\text{N}_4/\text{TiO}_2$ -HNB hybridized composite, photocurrent test was further performed. Usually, the value of photocurrent indirectly reflects the semiconductor's ability of generating and transferring of photo-generated charge carriers under irradiation [17]. Fig. 11 compares the photocurrent response of the photocatalysts coated on ITO electrodes in several on-off cycles. A prompt generation of photocurrents with good reproducibility were observed when ITO/ TiO_2 electrodes were illuminated. While the lamp is off, the values of photocurrent for all the ITO/ TiO_2 samples are instantaneously closed to zero. It can be clearly seen that the photocurrent decreases with the order of $\text{TB0.2} > \text{TB1} > \text{TB0}$, and the photocurrent value of TB0.2 electrode reached as high as 0.28 mA cm^{-2} , which is 27% time higher than that of pure TiO_2 -HNB (TB0). Consistent with the photocatalytic activity, modification of TiO_2 -HNB with too much $\text{g-C}_3\text{N}_4$ results in a decreased photocurrent (only 0.05 mA cm^{-2} for TB1), possibly due to the light-filtering effect. The study of Niu et al. suggested that $\text{g-C}_3\text{N}_4$ sheets can improve electron transport ability and increase the lifetime of photo-excited charge carrier [7]. Therefore, it is reasonable to see

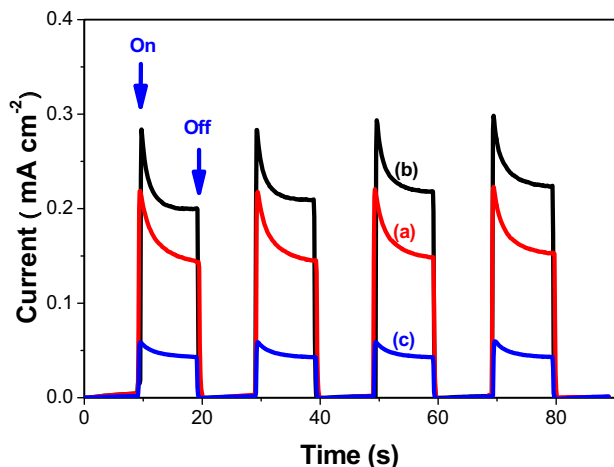


Fig. 11. Comparison of the transient photocurrent responses for TB0 (a), TB0.2 (b) and TB1 (c) photocatalysts.

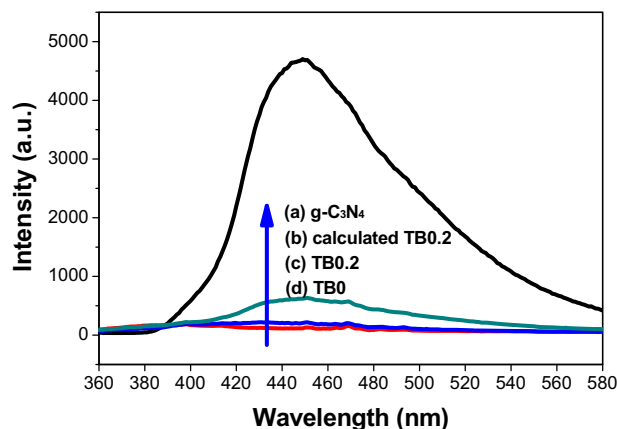


Fig. 12. Photoluminescence (PL) spectra of the as-prepared $\text{g-C}_3\text{N}_4$, TB0, TB0.2 samples, together with the calculated spectrum of TB0.2 based on the sum of the spectra of $\text{g-C}_3\text{N}_4$ and TB0 at their weight ratio.

the positive effect of $\text{g-C}_3\text{N}_4$ on the enlarged photocurrent response of TiO_2 -HNB.

Photoluminescence analysis can also be used to analyze the recombination rate of photo-generated carrier [25]. Herein, we also conducted PL measurement to study the effect of $\text{g-C}_3\text{N}_4$ on the recombination of photo-generated electron-hole pair of TiO_2 -HNB. It can be seen that $\text{g-C}_3\text{N}_4$ exhibits the strongest photoluminescence with an emission peak at about 447 nm (Fig. 12a), which is in accordance with UV-Vis DRS analysis (Fig. 7). This strong peak is attributed to the band-band PL phenomenon with the energy of light approximately equal to the band gap energy of $\text{g-C}_3\text{N}_4$ (2.7 eV) [22]. Compared with $\text{g-C}_3\text{N}_4$, the PL intensities of TB0 (Fig. 12d) and TB0.2 (Fig. 12c) are much weaker, reflecting their slow recombination rates of photo-generated electron-hole pairs. Although the PL intensity of TB0.2 is slightly higher than that of TB0, which is much weaker than that of calculated TB0.2, where the PL intensity of the calculated TB0.2 was obtained by summing up the PL spectrum of pure $\text{g-C}_3\text{N}_4$ and TiO_2 -HNBs (TB0) based on their weight ratios (Fig. 12b). The weaker intensity of TB0.2 than that of the calculated value suggests that the presence $\text{g-C}_3\text{N}_4$ can sharply reduce the recombination rate of the carriers due to the efficient removal of photo-generated electrons accumulated on (1 0 1) facets of TiO_2 -HNB by $\text{g-C}_3\text{N}_4$ (Fig. 1B).

3.8. Mechanism

Heterojunction-type photocatalytic system has been used to interpret the enhanced photocatalytic activity of $\text{g-C}_3\text{N}_4$ modified TiO_2 [10], where it was proposed the transferring of photogenerated holes from the VB of TiO_2 to the VB of $\text{g-C}_3\text{N}_4$, and the injecting of electrons from the CB of $\text{g-C}_3\text{N}_4$ to the CB of TiO_2 . If it is that case, the oxidation ability of photo-active $\text{g-C}_3\text{N}_4/\text{TiO}_2$ -HNB hybrid should be decided by the VB of $\text{g-C}_3\text{N}_4$. However, according to the study of Wang et al., the hole in the VB of $\text{g-C}_3\text{N}_4$ (1.4 V) is inadequate to oxidize $-\text{OH}$ to $\cdot\text{OH}$ radicals due to its low potential [9]. Based on the fact that the formation rate of $\cdot\text{OH}$ radicals is enhanced after modification of TiO_2 -HNB with $\text{g-C}_3\text{N}_4$, it seems that this Heterojunction-type model does not work in the present work.

Here, we believe that $\text{g-C}_3\text{N}_4$ acts as an electron reservoir to trap electrons emitted from TiO_2 -HNB, preventing the electron-hole pair from recombination. Therefore, $\text{g-C}_3\text{N}_4/\text{TiO}_2$ may act as a direct Z-scheme photocatalyst as shown in Fig. 13.

According to previous study [4–6], the (1 0 1) and (0 0 1) facets of anatase TiO_2 exhibit different band structures and band edge positions. Thus, the coexposed (1 0 1) and (0 0 1) facets of anatase can

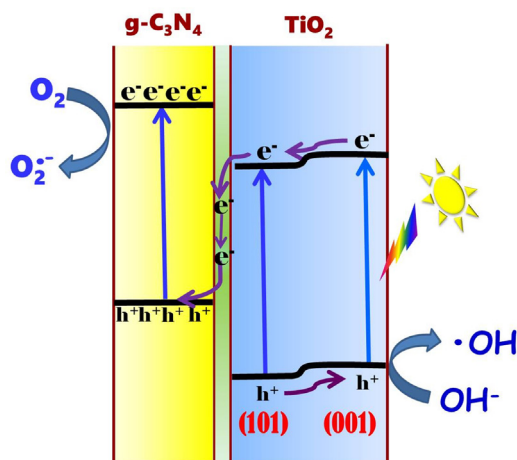


Fig. 13. Schematic illustration for the mechanism of photoinduced charge carrier transfers in g-C₃N₄/TiO₂-HNB hybrid under UV irradiation.

form a surface heterojunction within single TiO₂ particle, which is beneficial for the transfer of photogenerated electrons and holes to (101) and (001) facets, respectively. Under UV irradiation, the electrons accumulated on (101) facets of TiO₂-HNB then transfer to VB of g-C₃N₄, which are further excited to its CB, resulting in efficient spacial separation of the photo-induced charge carriers. Then, the electrons stored in the CB of g-C₃N₄ are trapped by O₂, forming reactive superoxide radical ions (O₂^{•−}), while the holes left in the (001) facets of TiO₂-HNB react with adsorbed water molecules (or surface hydroxyls) near the surface of TiO₂ to form •OH radicals. Finally, the X3B dye is oxidized due to the attack of reactive oxygen species (•OH and O₂^{•−} radicals). Quenching experimental results showed that both holes and O₂^{•−} radicals are main reactive oxygen species that responsible for the degradation of X3B (Fig. 10), where triethanolamine (TEOA, 0.01 M), *p*-benzoquinone (BZQ, 0.001 M) and isopropanol (IPA, 0.02 M) were employed as scavengers for photo-generated holes (h⁺), superoxide anion radicals (O₂^{•−}) and •OH radicals, respectively.

4. Conclusions

Not only band structures, but also contact interface between two semiconductors can affect the photocatalytic activity of hybridized photocatalyst. The unique structure of TiO₂-HNB makes it an ideal model to study the effect of contact interface on the photocatalytic activity of g-C₃N₄/TiO₂ hybrid. The photocatalytic activity of TiO₂-HNB was greatly enhanced by contacting g-C₃N₄ via (101)

facets due to efficient removal of photo-generated electrons accumulate on (101) facets of TiO₂. The prepared g-C₃N₄/TiO₂-HNB hybrid acts as a direct Z-scheme photocatalytic mechanism. The present study provides new idea in design of high-photoreactive multi-component semiconductor photocatalyst.

Acknowledgements

This work was supported by Program for New Century Excellent Talents in University (NCET-12-0668) and National Natural Science Foundation of China (21373275, 20977114, 51402161 & 21207117).

Appendix A. Supplementary data

Supplementary data associated with this article can be found, in the online version, at <http://dx.doi.org/10.1016/j.apcatb.2014.09.043>.

References

- [1] A. Kubacka, M. Fernandez-García, G. Colon, *Chem. Rev.* 112 (2012) 1555.
- [2] X.B. Chen, S.S. Mao, *Chem. Rev.* 107 (2007) 2891.
- [3] R.G. Li, F.X. Zhang, D. Wang, J.X. Yang, M.R. Li, J. Zhu, X. Zhou, H.X. Han, C. Li, *Nat. Commun.* (2013), <http://dx.doi.org/10.1038/ncomms2401>.
- [4] T. Ohno, K. Sarukawa, M. Matsumura, *New J. Chem.* 26 (2002) 1167.
- [5] N. Murakami, Y. Kurihara, T. Tsubota, T. Ohno, *J. Phys. Chem. C* 113 (2009) 3062.
- [6] J.G. Yu, J.X. Low, W. Xiao, P. Zhou, M. Jaroniec, *J. Am. Chem. Soc.* 136 (2014) 8839.
- [7] P. Niu, L.L. Zhang, G. Liu, H.M. Cheng, *Adv. Funct. Mater.* 22 (2012) 4763.
- [8] X.C. Wang, K. Maeda, A. Thomas, K. Takanabe, G. Xin, J.M. Carlsson, K. Domen, M. Antonietti, *Nat. Mater.* 8 (2009) 76.
- [9] F.Z. Su, S.C. Mathew, G. Lipner, X.Z. Fu, M. Antonietti, S. Blechert, X.C. Wang, *J. Am. Chem. Soc.* 132 (2010) 16299.
- [10] L.A. Gu, J.Y. Wang, Z.J. Zou, X.J. Han, *J. Hazard. Mater.* 268 (2014) 216.
- [11] J.G. Yu, S.H. Wang, J.X. Low, W. Xiao, *Phys. Chem. Chem. Phys.* 15 (2013) 16883.
- [12] X.S. Zhou, B. Jin, L.D. Li, F. Peng, H.J. Wang, H. Yu, Y.P. Fang, *J. Mater. Chem.* 22 (2012) 17900.
- [13] Z.A. Huang, Z.Y. Wang, K.L. Lv, Y. Zheng, K.J. Deng, *ACS Appl. Mater. Interfaces* 5 (2013) 8663.
- [14] Q.J. Xiang, K.L. Lv, J.G. Yu, *Appl. Catal. B* 96 (2010) 557.
- [15] Z.Y. Wang, K.L. Lv, G.H. Wang, K.J. Deng, D.G. Tang, *Appl. Catal. B* 100 (2010) 378.
- [16] J.H. Cai, Z.Y. Wang, K.L. Lv, Y. Zheng, J.G. Yu, M. Li, *RSC Adv.* 3 (2013) 15273.
- [17] K.L. Lv, X.F. Li, K.J. Deng, J. Sun, X.H. Li, M. Li, *Appl. Catal. B* 95 (2010) 383.
- [18] L. Chen, L.F. Shen, P. Nie, X.G. Zhang, H.S. Li, *Electrochim. Acta* 62 (2012) 408.
- [19] C.Z. Wen, Q.H. Hu, Y.N. Guo, X.Q. Gong, S.Z. Qiao, H.G. Yang, *Chem. Commun.* 47 (2011) 6138.
- [20] S.F. Xie, X.G. Han, Q. Kuang, J. Fu, L. Zhang, Z.X. Xie, L.S. Zheng, *Chem. Commun.* 47 (2011) 6722.
- [21] K.L. Lv, H.S. Zuo, J. Sun, K.J. Deng, S.C. Liu, X.F. Li, D.Y. Wang, *J. Hazard. Mater.* 161 (2009) 396.
- [22] S. Kumar, T. Surendar, A. Baruah, V. Shanker, *J. Mater. Chem. A* 1 (2013) 5333.
- [23] K.L. Lv, J.G. Yu, K.J. Deng, X.H. Li, M. Li, *J. Phys. Chem. Solids* 71 (2010) 519.
- [24] L.L. Si, Z.A. Huang, K.L. Lv, D.G. Tang, C.J. Yang, *J. Alloys Compd.* 601 (2014) 88.
- [25] K.L. Lv, J.C. Hu, X.H. Li, M. Li, *J. Mol. Catal. A* 356 (2012) 78.